Chemical Engineering Journal 519 (2025) 165084

Contents lists available at ScienceDirect

Chemical Engineering Journal

journal homepage: www.elsevier.com/locate/cej

Synergistic effects of shell-hollow confinement catalysis in Au@Cu_2O nanoreactors toward efficient electrocatalytic CO_2 to multi-carbon products

Wenqing Chu [a], Guangxin Sun [b], Zheng Chen [a], Xiongwei Tian [a], Shun Wang [a], Mengyin Xie [a], Ruoyu Wu [a], Haijiao Xie [d], Yuqun Zhuo [a,c,e,*]

[a] Department of Energy and Power Engineering, Key Laboratory for Thermal Science and Power Engineering of the Ministry of Education, Tsinghua University, Beijing 100084, China
[b] Department of Materials Science and Engineering, National University of Singapore, Singapore, Singapore
[c] Beijing Engineering Research Center for Ecological Restoration and Carbon Fixation of Saline-alkaline and Desert Land, Beijing 100084, China
[d] Hangzhou Yanqu Information Technology Co., Ltd, Hangzhou, Zhejiang 310003, China
[e] Shanxi Research Institute for Clean Energy, Tsinghua University, Shanxi, Taiyuan 030000, China

ARTICLE INFO

Keywords:
Electrochemical CO_2 reduction
C_{2+} products
Yolk-shell nanoreactors
Shell-hollow ratio
CO coverage

ABSTRACT

Electrochemical CO_2 reduction reaction is a promising approach to converting CO_2 to high-value multi-carbon chemicals. Bimetallic yolk-shell nanoreactors for CO_2RR serve as an optimal platform for multi-component sequential reactions. However, the synergistic influence of tailoring shell thickness and hollow size on the diffusion, CO coverage, and dimerization of reaction intermediates remains inadequately elucidated. Herein, employing the Ostwald ripening method, a series of Au@Cu_2O nanoreactors with a 15 nm Au nanoparticle and a tunable shell-hollow are designed to facilitate tandem catalysis for CO_2RR. The Au@Cu_2O-1 with optimized shell-hollow ratio exhibits the highest selectivity of C_{2+} up to 76.08% at a total current density of 500 mA cm^{-2} in 1 M KOH electrolyte. Finite element simulations reveal that an optimized shell-hollow size ratio effectively balances CO_2 and CO mass transport within the shell and simultaneously maximizes *CO coverage on Cu_2O to promote efficient C-C coupling. In attenuated total reflection surface-enhanced infrared absorption spectroscopy analysis and density functional theory calculations demonstrate that the formation of bridged CO species and targeted CO coverage on the Cu surface significantly lower the energy barrier of the formation of *CHOCO. This study reveals an efficient Cu-based catalyst for CO_2RR, highlighting the importance of the synergistic effects of shell-hollow confinement catalysis.

1. Introduction

The consumption of fossil fuels and the excessive emission of CO_2 due to human activities have raised significant concerns regarding the energy crisis and environmental degradation [1]. Electrochemical CO_2 reduction reaction (CO_2RR) provides a promising pathway to achieve “carbon-neutral” economy by converting CO_2 into value-added chemicals and fuels using renewable electricity [2–4]. Among the various products obtained in the CO_2RR process, multi-carbon products (C_{2+} products) have attracted extraordinary interest owing to their advantages of high-energy density, higher chemical value, and broader application instead of C_1 products [5,6]. To date, Copper (Cu) has earned the distinction of being the only catalyst capable of converting CO_2 into C_{2+} products, mainly due to its moderate adsorption strength of *CO intermediate [7]. However, without any standardized design, Cu has hindered the efficient formation of C_{2+} products with high selectivity and activity stemming from sluggish kinetics of multi-proton coupled electron transfer and C-C coupling steps.

Various research has been directed toward designing Cu-based catalysts to achieve superior selectivity and activity for C_{2+} products, supported by advanced theoretical calculations to uncover the critical mechanistic steps within the reaction pathway [8,9]. It has been widely accepted that C-C coupling is the rate-determining step for the formation of C_{2+} products and CO is the key intermediate toward C-C coupling [10–12]. Improving *CO coverage on the catalyst surface is instrumental. Higher *CO coverage can not only promote C-C coupling but

---

* Corresponding author at: Department of Energy and Power Engineering, Key Laboratory for Thermal Science and Power Engineering of the Ministry of Education, Department of Energy and Power Engineering, Tsinghua University, Beijing 100084, China.

E-mail address: zhuoyq@tsinghua.edu.cn (Y. Zhuo).

https://doi.org/10.1016/j.cej.2025.165084
Received 19 March 2025; Received in revised form 28 May 2025; Accepted 17 June 2025

also restrict the competing hydrogen evolution reaction (HER) by substituting H* with CO* coverage according to DFT calculations and experimental certifications [13–17]. Recently, tandem structures have been considered as an effective methods toward the formation of specific products via stabilizing and enriching CO intermediate. In detail, the metals such as Ag [18–20], Au [21,22], and Zn [23,24], which is easy to activate CO_2 to form CO, are commonly employed to combined with Cu for producing CO species effectively. The generated CO subsequently diffuses to the Cu, which improving the *CO coverage on the Cu surface and thus reducing the energy barrier of CO dimerization, boosting the C_{2+} products formation. However, this easy tandem open model leads to the rapid migration or diffusion of in situ-generated CO into the gas phase due to the mismatch between the CO generation rate and the C-C coupling rate, thereby hindering the subsequent coupling of *CO intermediates. Therefore, it is imperative to restrict CO desorption to facilitate the reaction. The confined model can restrict CO desorption from the catalyst surface, balance CO flux, and promote C-C coupling. This represents a more practical design to achieve high C_{2+} selectivity through spatially constrained tandem reaction flow [25–29]. Therefore, constructing the confined nano-reactor tandem system represents a more effective design to achieve high C_{2+} selectivity through regulating tandem reaction flow [30].

Several studies have made commendable efforts to elucidate the factors influencing the C_{2+} formation in cascade nanoreactors. It has been found that the product selectivity of CO_2RR is related to the shell thickness, where well-calibrated shell thickness can achieve optimal progress of diffusion and dimerization of reaction intermediates to maximize the Faradaic efficiency (FE) of C_{2+} (FE_{C2+}) [31–33]. Apart from optimizing the shell thickness, the hollow structure can also play essential roles in promoting C_{2+} selectivity. It is revealed that the hollow structure significantly increases *CO coverage, thereby stabilizing Cu^+ species against reduction and facilitating the selective production of C_{2+} products [27]. Additionally, in a Cu_2O-derived hollow hierarchical structure for CO_2RR, the hollow structure can not only locally concentrate CO within the hollow region to increase *CO coverage but also enhance the local pH and electric field [34]. Furthermore, a self-pressurizing nanoscale capsule catalyst blocks the CO inside the capsule structure, creating a high-pressure and high-concentration CO intermediate environment. The DFT calculation results suggest that higher *CO coverage on the catalyst surface restricts the competing hydrogen evolution reaction (HER) by substituting H* with CO* coverage, thereby enhancing C-C coupling and improving the yield of acetate or propanol products [17]. These studies indicate that both shell thickness and hollow size significantly influence C_{2+} production. While shell thickness and hollow size impose confinement effects, they also optimize the diffusion and transport of CO_2 and CO within the shell, facilitating the coupling of CO intermediates. However, these investigations primarily focus on the individual effects of shell thickness or hollow size. Their synergistic impacts on the C_{2+} formation have been understudied. Furthermore, the precise roles of fine-tuning shell thickness and hollow size on the diffusion, CO coverage, and dimerization of reaction intermediates remain insufficiently understood.

In this work, we synthesized Au@Cu_2O yolk-shell-structured catalysts featuring tunable shell thicknesses and hollow sizes by employing the principles of Oswald ripening. A series of Au@Cu_2O catalysts are prepared with shell-hollow size ratios of 2.90, 1.84, and 1.42, designated as Au@Cu_2O-0.5, Au@Cu_2O-1 and Au@Cu_2O-2, respectively. Notably, the Au@Cu_2O-1 with optimal Cu_2O shell and hollow size demonstrates excellent catalytic activity and C_{2+} product selectivity, achieving a FE_{C2+} of 76.08% under the total current density of 500 mA cm^{-2} at an applied potential of -1.06 V versus Reversible Hydrogen Electrode (vs. RHE). In situ spectroscopy revealed that the Au@Cu_2O-1 structure strengthened CO adsorption and facilitated the formation of bridged CO species, which is conducive to enhancing C-C coupling. The combined results of characterization and theoretical calculation have proved that the structure of shell-hollow Au@Cu_2O-1 could restrict *CO desorption and enrich *CO coverage on the Cu surface, thus lowering the energy barrier of CO dimerization to produce C_{2+} products efficiently.

2. Experiment section

2.1. Materials

Hydrogen tetrachlorocuprate (III) trihydrate ($HAuCl_4 \cdot 3H_2O$, 99.99%), citric acid, trisodium salt (98%), copper (II) nitrate trihydrate ($Cu(NO_3)_2 \cdot 3H_2O$, 99%), hydrazine solution ($N_2H_4 \cdot H_2O$, 85 wt%), polyvinylpyrrolidone (PVP, average M.W 58000), Potassium hydroxide (KOH, AR), Ethanol (AR) , Isopropanol (AR), Nafion (5%).All chemicals were used after being purchased from commercial suppliers without additional purification. Water purified with a Milli-Q system was used throughout the study; the resistivity is no <18.2 MΩ·cm.

2.2. Synthesis of catalysts

The seed growth and Ostwald ripening synthesis process was modified slightly to synthesize the Au@Cu_2O cascade nanoreactors [35].

Synthesis of Au core: The Au NPs with a diameter of about 15 nm were synthesized and used as the core materials for the Au@Cu_2O yolk-shell particle fabrication. Au NPs were prepared by a standard citrate reduction procedure. Typically, 150 mL of 0.025 M $HAuCl_4$ solution was added into a three-necked round bottom flask and heated to boiling under continuously magnetic stir with condensing and refluxing conditions. Then 7.5 mL of 0.02 M sodium citrate solution was added. After reaction for 30 min, heating resource was removed and the solution was allowed to cooled down naturally to room temperature. Finally, the solution was titrated with deionized water to a final volume of 200 mL to obtain the Au NP colloidal solution.

Synthesis of Au@Cu_2O yolk-shell catalysts: Au@Cu_2O yolk–shell NPs was prepared by hydrazine hydration reduction method. Typically, 3 g of PVP powders was added into 150 mL of 0.01 M $Cu(NO_3)_2$ solution under constant stirring until the PVP powders were dissolved completely. Then a certain amount (0.5, 1, 2 mL) of as-obtained Au NPs solution was added, followed by immediate introduction of 17 μL trace hydrazine hydrate. After 10 min of reaction, the Au@Cu_2O yolk–shell NPs were synthesized and centrifuged (10,000 rpm), washed four times with water and ethanol, and then dried in an oven at 60 °C for later use. Au@Cu_2O NPs with different shell-to-hollow thickness ratio can be controlled through adjusting the amount of reducing agent.

Synthesis of Cu_2O NPs: 3 g of PVP powders were added into 150 mL of 0.01 M $Cu(NO_3)_2$ solution under constant stirring until the PVP powders were dissolved completely, followed by immediate introduction of 17 μL trace hydrazine hydrate. After 10 min of reaction, the Cu_2O NPs were synthesized and centrifuged (10,000 rpm), washed four times with water and ethanol, and then dried in an oven at 60 °C for later use.

2.3. Characterization of catalysts

The as-synthesized Au@Cu_2O and Cu_2O were characterized by various analytical techniques. The morphology of the samples was observed by scanning electron microscopy (SEM, Merlin ZEISS) and transmission electron microscopy (TEM, JEM2010). High resolution transmission electron microscopy (HRTEM) and energy-dispersive X-ray (EDX) elemental mapping studies were conducted on a JEOL-2010F TEM with acceleration voltage of 200 kV. X-ray diffraction (XRD) was performed on a Rigaku Smart Lab 3KW X-ray diffractometer with Cu-Kα radiation ($\lambda = 1.54178$ Å). The X-ray photoelectron spectroscopy (XPS) measurements were performed on a ESCALAB 250Xi of Thermo Fisher X-ray photoelectron spectrometer with Mg Kα X-ray and Al Kα X-ray as the exciting source. The C 1 s peak at 284.8 eV was used as a reference to correct for charging effects.

2.4. Electrochemical measurements

The electrochemical measurements were conducted with an electrochemical workstation (Interface 1010, Shanghai Gamry Instruments). The Ag/AgCl wire in saturated KCl solution was adopted as the reference electrode, and the counter anodic reaction was oxygen evolution reaction over a Ni foam. All potentials were converted to the RHE reference scale using the relation $E_{RHE} = E_{Ag/AgCl} + 0.197 + pH\times 0.059$ and compensated for the solution resistance by 85%.

2.4.1. Electrochemical performance tests

To prepare a catalyst electrode for a flow cell test, 54 mg of catalyst, mixed with 360 μL of Nafion in 18 mL of isopropanol, was deposited on a carbon gas diffusion layer (GDL, YLS-30 T) after oscillating 0.5 h to form a uniform catalyst ink, which was bought from Sheng'erno Energy Mall. The catalyst-loaded GDL, anion exchange membrane (FAB-PK-130) and nickel foam anode were assembled using polyethylene gaskets and separated by chambers filled with electrolyte for the cathode and anode, respectively. The 1 M KOH electrolyte was pumped and circulated through both the anode and cathode chambers. Then CO_2 flowed through gas room behind the cathode. The CO_2 inlet flow rate was kept at 30 sccm while the electrolyte flow rate was kept at 15 mL min^{-1}.

Samples were collected every 7.5 min after an initial 5-min electrolysis period, and the gaseous products from CO_2RR were analyzed using an online gas chromatograph (Agilent 8860). A thermal conductivity detector (TCD) was used to examine H_2 and CO. Using a flame ionization detector (FID), hydrocarbons (CH_4 and C_2H_4) were examined. A standard curve was established by testing the peak integration areas of various gaseous products at different concentrations under identical injection flow rates. Quantification of gaseous products during the testing process was performed using the external standard method. The Faradaic efficiency of the gaseous products was calculated using the following formula:

$$FE_{gas} = i_{gas}/i_{total}*100\% = V_{gas}*\nu*p_0*N*F/(R*T*i_{total})*100\%$$

where i_{total} - Total current; i_{gas} - Partial current corresponding to the gaseous product; ν - The outlet flow rate of the outlet mixture gas (measured by an Agilent ADM flowmeter G6691A at the GC inlet/reactor outlet); p_0 - Atmospheric pressure ; R - Ideal gas constant; T - Room temperature; N - Number of electrons transferred per product molecule; F - Faraday constant.

Liquid products were collected every 20 min and quantified using an external standard method with a 400 MHz Nuclear Magnetic Resonance (NMR) spectrometer (JEOL ECS-400) through ^1H NMR analysis. Using a method for water suppression, NMR spectrometer was used to detect the liquid products such as HCOOH, C_2H_5OH, CH_3COOH and $CH_3CH_2CH_2OH$.

The Faradaic efficiency (FE) of the liquid products was determined using the following formula:

$$FE_{liquid} = c*V*N*F/C*100\%$$

where c - Concentration of the liquid product, calculated from the peak area and the external standard curve; V - Volume of the electrolyte; N - Number of electrons transferred per product molecule; F - Faraday constant; C - Total charge passed through the working electrode per unit time.

2.4.2. Electrochemical analysis

The reactor assembly is consistent with that described in Section 2.4.1. Electrochemical Performance Tests. All experiments were conducted in 1 M KOH solution. The linear sweep voltammetry (LSV) was performed in CO_2 at a scan rate of 5 mV s^{-1}. The double-layer capacitance (C_{dl}) was measured using cyclic voltammetry (CV) at various scan rates from 20 mV s^{-1} to 120 mV s^{-1} to determine the electrochemically active surface area (ECSA). The electrochemical impedance spectra (EIS) were measured using an applied AC voltage of 5 mV amplitude at −2.2 V (vs Ag/AgCl) and a frequency range of 1000 kHz to 1 Hz.

3. Results and discussion

3.1. Nanostructure and morphology analysis

Yolk-shell structured catalysts, designated as $Au@Cu_2O$-x (where x denotes the volume of the Au colloidal solution utilized during the reaction-0.5 mL, 1 mL, 2 mL), were synthesized using seed growth and Ostwald ripening strategies. These structures consist of Au nanosphere-like “a yolk or core” encased within spherical cavities of Cu_2O “a shell.” $Au@Cu_2O$ nanoreactors was composed of Au yolk, hollow region and Cu_2O shell. The morphology analysis was subjected to systematic investigation through various characterization techniques.

Based on the transmission electron microscopy (TEM) image (Fig. S1a) and particle size analysis (Fig. S1b), the Au nanoparticles exhibited uniform size and spherical morphology with an average diameter of 15 nm. According to the scanning electron microscopy (SEM) and TEM images, and particle size analysis (Figs. 1a and S2-S4) of $Au@Cu_2O$ nanoreactors, the mean total particle diameter of $Au@Cu_2O$-0.5, $Au@Cu_2O$-1, $Au@Cu_2O$-2 nanoreactors are 143, 107, 66 nm. It was observed that as the volume of Au colloid increased, there was a deterioration in surface smoothness, enlargement of internal hollowness, and a progressive loosening of the shell structure accompanied by an increase in porosity. When no Au colloid was added (Fig. S5) (corresponding to the Cu_2O nanoreactors), the mean total particle diameter is 629 nm. The structure's overall size and the hollow region expanded. The shell maintained a smooth surface with minimal porosity. Furthermore, the yolk-shell separated structure of the $Au@Cu_2O$-1 nanoreactor was verified through high-resolution transmission electron microscopy (HRTEM) imaging, supplemented by energy dispersive X-ray spectroscopy elemental mapping and line-scan analysis as presented in the supporting information (Fig. 1b, c and Fig. S6). As illustrated, the yolk was delineated by the Au signal, while the shell was composed of Cu and O. Furthermore, HRTEM images disclosed an interplanar spacing of 0.23 nm of the core nanoparticles, corresponding to the (111) crystallographic plane of metallic Au [36]. In contrast, the shell exhibited an interplanar spacing of 0.25 nm with the characteristic of the (111) facet of Cu_2O [37].

Based on Fig. 1d-f and Fig. S7, the hollow thicknesses of $Au@Cu_2O$-0.5, $Au@Cu_2O$-1, $Au@Cu_2O$-2, Cu_2O nanoreactors were 34.05, 41.38, 28.74, 217.86 nm and the shell thicknesses were 98.71, 76.29, 40.92, 313.57 nm. The shell-hollow ratio was calculated using the formula:

$$\text{shell - hollow ratio} = (\text{total diameter}/\text{hollow diameter}) - 1$$

Therefore, the shell-hollow size ratios were measured as 2.90, 1.84, and 1.42, 1.44 respectively.

To further verify the elemental composition and valence states of $Au@Cu_2O$ yolk-shell nanoreactors, X-ray photoelectron spectroscopy (XPS) analysis was conducted. The Au 4f spectra (Fig. S8a, yellow area) showed weak peak intensity [38]. The survey XPS spectra showed the presence of only Au, Cu, and C elements (Fig. S8b). Cu 2p XPS spectra (Fig. 1g, dark blue and orange regions) and Cu LMM Auger spectrum (Fig. 1h, blue regions) validated the presence of Cu_2O, with the weak satellite peaks in the Cu 2p spectrum suggesting slight oxidation of Cu_2O under ambient conditions, resulting in the formation of a small amount of CuO [39]. The peak of Cu $2p_{3/2}$ shifted from 931.4 eV (Cu_2O NPs) to 932.09 eV ($Au@Cu_2O$-2), 931.87 eV ($Au@Cu_2O$-1) and 932.00 eV ($Au@Cu_2O$-0.5). And a slight positive shifted in the Cu $2p_{1/2}$ binding energy is observed, increasing from 951.23 eV for Cu_2O to 951.93 eV in the $Au@Cu_2O$-2. As the electron donor, the energy binding of Cu increased. These changes of binding energy positions could be explained by the interphase electron transfer from Cu to Au atoms [40–42]. Moreover, the formation of electron-deficient Cu sites generated from the interphase electron transfer from Cu to Au atoms would stabilize Cu^+

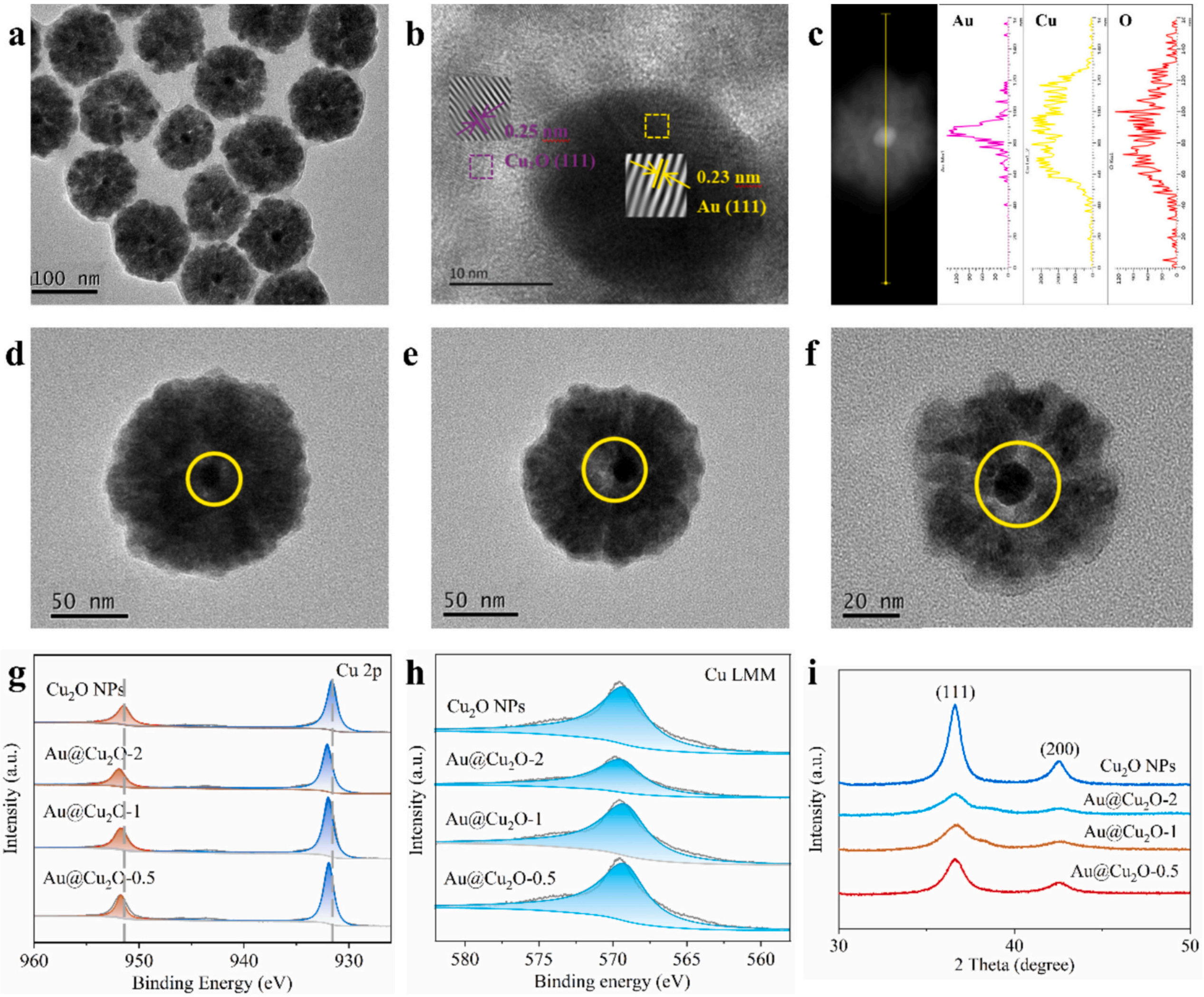

Fig. 1. (a) SEM and (b) HRTEM image with crystallographic plane spacing determination and interplanar distance analysis of Au@Cu_2O-1 NPs. (c) line scanning of Au@Cu_2O-1 NP. TEM images of (d) Au@Cu_2O-0.5 NP with a shell-hollow size ratio of 2.90, (e) Au@Cu_2O-1 NP with a shell-hollow size ratio of 1.84, (f) Au@Cu_2O-2 NP with a shell-hollow size ratio of 1.42. The yellow circles represent the hollow regions within each structure. The XPS of (g) Cu 2p, (h) Cu LMM, and (i) the XRD of the as-prepared Au-Cu_2O-1 NPs.

and favor the adsorption of *CO intermediates [43–45]. X-ray diffraction (XRD) analysis provided additional insights into the crystal structure and phase composition of Au@Cu_2O yolk-shell nanoreactors, as depicted in Fig. 1i. The diffraction peaks at 36.5° and 42.4° were assigned to the (111) and (200) planes of cubic Cu_2O, respectively [29]. Due to the relatively low Au content and its confinement within the Cu_2O shell, the peak intensity of Au was not discernible in the XRD patterns. Overall, the successful synthesis of the Au@Cu_2O nanoreactors was confirmed through the aforementioned characterization techniques.

To investigate the morphology and structure of Cu_2O after the electrochemical reaction, we performed SEM and XPS tests on the Au@Cu_2O-1 nanoreactors following 10 min of catalytic reaction. As shown in Fig. 2a, b, and Fig. S9, the spherical structure of Au@Cu_2O-1 remains virtually unchanged before and after the reaction [44,46–49]. However, the amount of the surface binder Nafion was slightly reduced, likely due to its removal by the flow of the electrolyte, which is a typical phenomenon [50,51]. The Cu 2p spectra of the Au@Cu_2O-1 catalytic electrode before and after the catalytic reaction are shown in Fig. 2c. It was revealed that new peaks appeared at 953.73 eV for the Cu $2p_{1/2}$ and at 934.25 eV for the Cu $2p_{3/2}$, corresponding to metallic Cu^0 [52–54]. Therefore, during the catalytic process, a small portion of Cu_2O is reduced to Cu, while the majority of Cu_2O remains intact. This suggests that the Cu_2O component in the catalysts maintained a stable structure following the catalytic reaction. The Cu LMM spectra of the Au@Cu_2O-1 catalytic electrode before and after the catalytic reaction, shown in Fig. 2d, mostly corresponded to Cu^+, with a smaller portion corresponding to Cu^0. This supported the conclusion obtained from the Cu 2p spectra that the Cu_2O shell remained stable during the catalytic process. From Fig. 2c, the peak of Cu $2p_{3/2}$ shifted from 931.4 eV (Cu_2O NPs) to 931.79 eV (Au@Cu_2O-1-after). And a slight positive shifted in the Cu $2p_{1/2}$ binding energy is observed, increasing from 951.23 eV for Cu_2O to 951.64 eV in the Au@Cu_2O-1-after. These changes in binding energy positions indicate that the structure after the catalytic reaction also reflects the interphase electron transfer from Cu to Au atoms. The inherent mechanism responsible for the stability of the Cu_2O shell during the catalytic reaction has also been extensively studied by numerous researchers. They found that both the shell structure and the introduction of Au play a role in stabilizing Cu^+ [27,44,46,47,55,56].

Therefore, the Au@Cu_2O nanoreactors were successfully fabricated, and their ability to maintain structural stability during the catalytic process provides a solid foundation for the catalytic reaction.

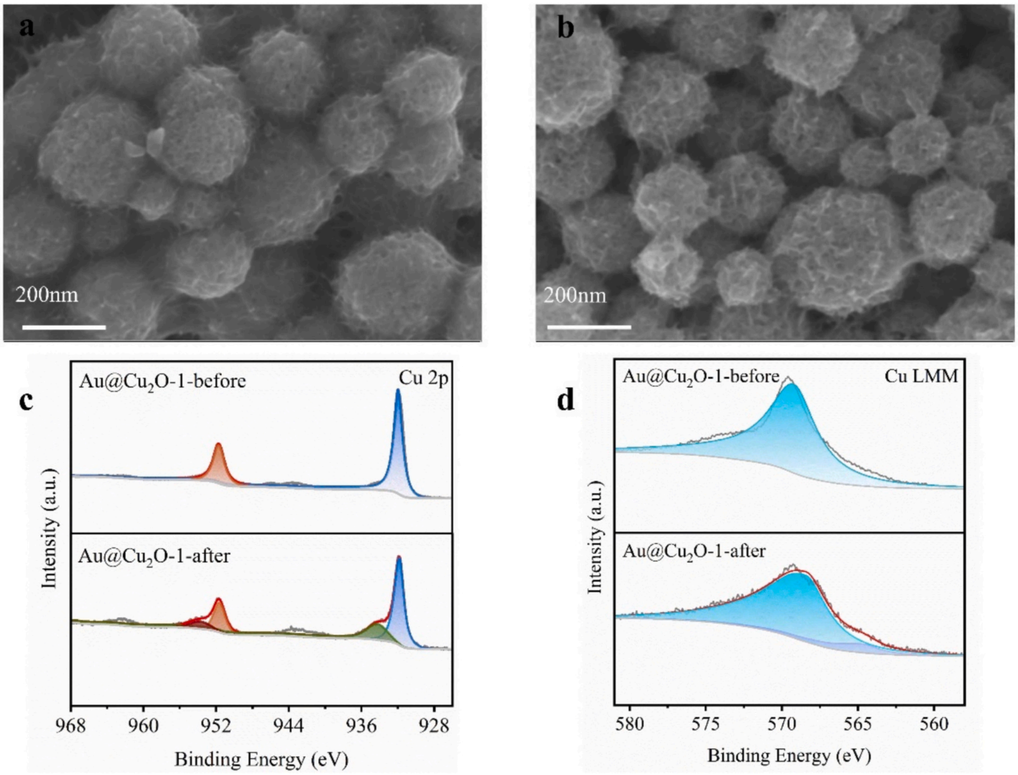

Fig. 2. SEM of Au@Cu_2O-1 NPs (a) before catalytic reduction (10 min) and (b) after catalytic reduction (10 min), (c) Cu 2p spectra of Au@Cu_2O-1 NPs before and after catalytic reduction (10 min), (d) Cu LMM Auger spectra of Au@Cu_2O-1 NPs before and after catalytic reduction (10 min).

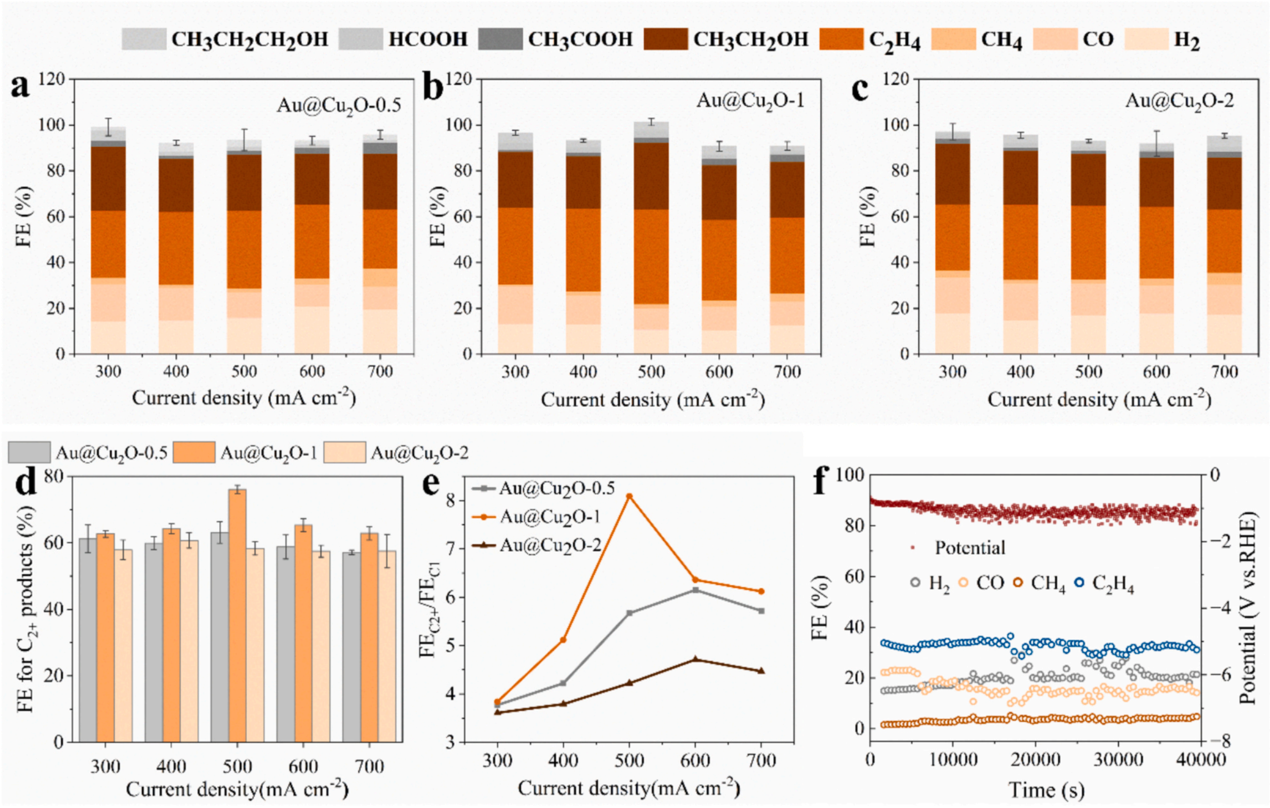

Fig. 3. FE of all products at various current densities for (a) Au@Cu_2O-0.5 NPs, (b) Au@Cu_2O-1, and (c) Au@Cu_2O-2 NPs. (d) FE for C_{2+} products, (e) The ratios of FE_{C2+} to FE_{C1} for Au@Cu_2O nanoreactors under different current densities, (f) stability test of Au@Cu_2O-1 NPs at the current density of 300 mA cm^{-2}.

3.2. CO_2RR performance

The catalytic performance of Au@Cu_2O yolk-shell nanoreactors for CO_2RR was systematically examined in a flow cell employing 1 M KOH as the electrolyte. Before the CO_2RR evaluation, all catalysts were subjected to linear sweep voltammetry (LSV) tests (Fig. S10). Compared to pristine Cu_2O hollow nanoparticles, Au@Cu_2O nanoreactors demonstrated a lower onset potential and higher current density at the same potential, indicating enhanced catalytic activity. Furthermore, Au@Cu_2O-1 showed the lowest Tafel slope value of 4.11 among the Au@Cu_2O nanoreactors, indicating the fastest surface reaction kinetics and highest catalytic activity (Table S1). Following the catalytic activity comparison via LSV, chronoamperometric tests were conducted to assess the selectivity of catalysts across various current densities, thereby providing a deeper evaluation of their overall performances. Notably, Au@Cu_2O-1 exhibited the highest C_{2+} product selectivity (Fig. 3b) with a shell-hollow ratio of 1.84, achieving a peak FE of 76.08%, comprising 41.32% C_2H_4, 29.20% C_2H_5OH, 2.02% CH_3COOH, and 3.53% $CH_3CH_2CH_2OH$ at a current density of 500 mA cm^{-2}. Compared to Au@Cu_2O-1, Au@Cu_2O-0.5 with a shell-hollow ratio of 3.9 reached a maximum FE of 63.10% at 500 mA cm^{-2} (Fig. 3a), while Au@Cu_2O-2 with a shell-hollow ratio of 2.42 achieved a FE of 58.31% at 500 mA cm^{-2} (Fig. 3c).

Through the performance comparison, catalysts with different shell-hollow ratios exhibited associated selectivity, likely due to the synergistic effects of shell thickness and hollow size. Shell thickness influenced CO_2 diffusion into the hollow region and affected the CO generation on the Au nanoparticles. Additionally, Shell thickness increased the diffusion resistance of CO formed on the Au nanoparticles as CO exited the shell and promoted the CO coupling process on the Cu_2O shell during diffusion. Hollow size impacted the diffusion of both CO_2 and CO and provided spatial opportunities to facilitate CO production on Au nanoparticles, thereby modulating CO concentration within the hollow region and further improving CO coverage on the Cu_2O shell surface. Consequently, we argued that the shell-hollow ratios played a crucial role in governing the relative diffusion dynamics of CO_2 and CO, CO coverage, as well as the kinetics of the C-C coupling reaction on the shell surface. Therefore, the shell-hollow ratio of 1.84 might ensure the most efficient mass transport of CO_2 and CO while concentrating CO into hollow region and promoting the CO coverage on the Cu_2O surface for C-C coupling. To further verify the influence of shell-hollow ratios, the C_{2+} selectivity, as well as the FE_{C2+}/FE_{C1} ratios of Au@Cu_2O nanoreactors, were compared under different current densities. In comparison with Au@Cu_2O-0.5 and Au@Cu_2O-2 nanoreactors, Au@Cu_2O-1 nanoreactor demonstrated a significantly enhanced ability to promote C_{2+} production, with its FE_{C2+} higher than the other nanoreactors at any current density (Fig. 3d). As depicted in Fig. 3e, ratios of the Au@Cu_2O-1 nanoreactor consistently outperformed the two comparative nanoreactors under all current densities, highlighting the pivotal influence of an optimized shell-hollow ratio on effectively facilitating the conversion of more CO into C_{2+} product. In summary, the shell-hollow ratios were crucial in promoting C_{2+} formation during CO_2RR.

To better evaluate the intrinsic activity of Au@Cu_2O NPs, the partial current density of C_{2+} was normalized by electrochemically active surface area (ECSA). The ECSA was first evaluated by calculating the electrochemical double-layer capacitance (C_{dl}) from cyclic voltammetry (CV) curves at various scan rates (Fig. 4a-d). The C_{dl} values for Cu_2O hollow NPs, Au@Cu_2O-0.5, Au@Cu_2O-1, and Au@Cu_2O-2 were measured as 0.97, 1.33, 0.6, and 1.21 mF cm^{-2}, respectively (Fig. 4e).

The normalized C_{2+} current density analysis indicated that the Au@Cu_2O-0.5 and Au@Cu_2O-2 nanoreactors exhibited lower intrinsic activity but higher selectivity than Cu_2O, which could be attributed to the incorporation of Au (Table S2 and Fig. S11). Among all catalysts, the Au@Cu_2O-1 nanoreactor achieved the highest intrinsic activity. Furthermore, under a total current density of 500 mA cm^{-2}, the normalized C_{2+} current density of the Au@Cu_2O-1 nanoreactor was 2.67 times that of Au@Cu_2O-0.5 and 2.63 times that of Au@Cu_2O-2.The

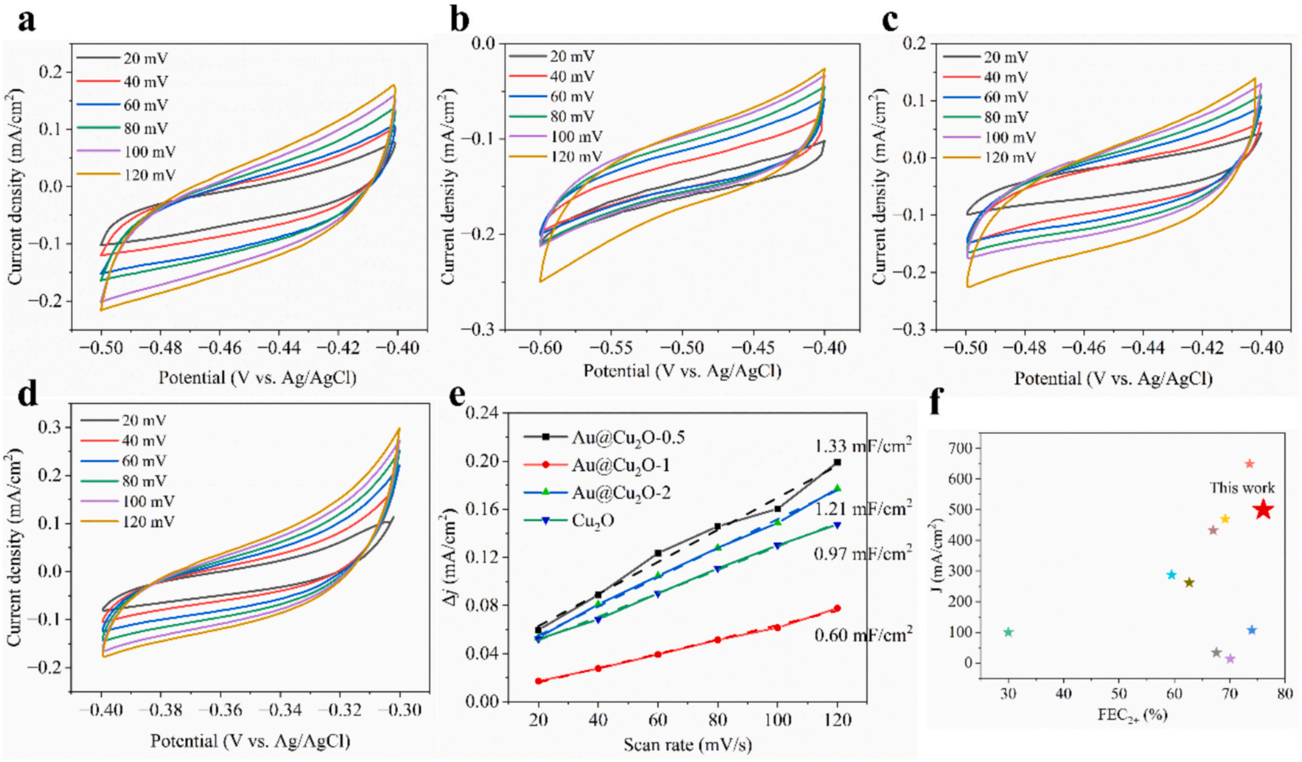

Fig. 4. CV voltammetry curves of (a) Au@Cu_2O-0.5, (b) Au@Cu_2O-1, (c) Au@Cu_2O-2, (d) Cu_2O nanoreactors recorded in 1 M KOH solution in CO_2 atmosphere at the scan rates ranging from 20 to 120 mV s-1, respectively, (e) Current density as a function of the scan rate for Au@Cu_2O-0.5, Au@Cu_2O-1, Au@Cu_2O-2, Cu_2O nanoreactors, (f) Performance comparison toward C_{2+} products with previous reports on CO_2RR using tandem or yolk-shell catalysts.

strengthened catalytic performance of the Au@Cu_2O-1 nanoreactor was primarily rooted in the optimization of the shell-hollow ratios. To examine the ability of the Au@Cu_2O-1 nanoreactor to preserve its superior performance, the stability test was evaluated under 300 mA cm^{-2}. The applied potentials and FE remained stable over 11 h (Fig. 3f). The relationship between current and voltage was further detailed in Fig. S12. At any tested current density, the Au@Cu₂O-1 nanoreactors showed the lowest voltage. This indicates that, at the same voltage, they achieved a higher current density, resulting in a faster reaction and minimal resistance during the process. A comparison of key performance metrics (Table S3 and Fig. 4f), including FE_{C2+}, current density, and potential (vs. RHE), revealed that the Au@Cu_2O-1 nanoreactor exhibited superior performance in CO_2RR to C_{2+} products, outperforming previously reported Au-Cu catalysts. This enhancement was partially attributed to its accelerated surface reaction kinetics and higher catalytic activity, as confirmed by linear sweep voltammetry (LSV) and cyclic voltammetry (CV) measurements, the fundamental reason lay in its uniquely tailored yolk-shell architecture with an optimized shell-to-hollow size ratio. This structural design delicately balanced CO_2 diffusion and CO intermediate retention within the confined shell space, thereby promoting *CO accumulation and facilitating subsequent C-C coupling at the Cu_2O surface.

3.3. Synergistic effects of shell-hollow confinement catalysis

3.3.1. Monitoring reaction intermediates via in-situ spectroscopy

To better understand the reaction mechanism of Au@Cu_2O catalyst, we first analyzed the reaction intermediates during the electrolysis of Au@Cu_2O-1 nanoreactor under different potentials using in situ Raman spectroscopy. The results indicated that, within the potential range of −0.2 V to −1.8 V (vs. RHE), the Raman spectra exhibited persistent peaks at 527 and 623 cm^{-1}, which were attributed to Cu_2O (Fig. S13) [26]. Notably, the peak intensity remained largely invariant with increasing potential, suggesting the effective preservation of Cu^+ during electrolysis. The retention of Cu^+ in hollow structures could be attributed to the elevated CO concentration [27]. Accordingly, it was hypothesized that the retention of Cu^+ observed in this study arose from the increased CO concentration. This may be attributed to the

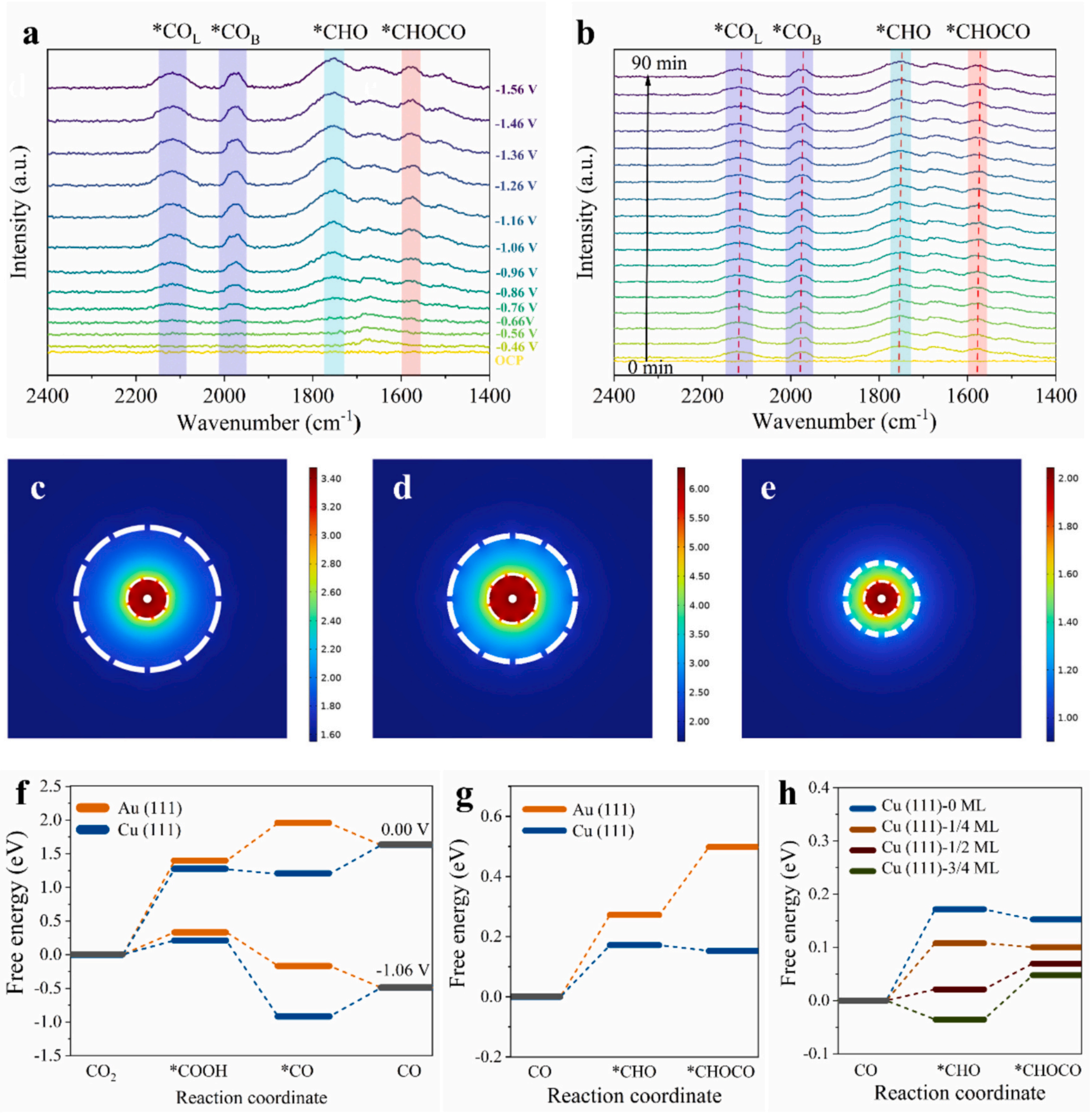

Fig. 5. ATR-SEIRAS of (a) at OCP and applied potentials from −0.46 to −1.56 V (vs. RHE); (b) at −1.06 V (vs. RHE) with reaction times from 0 to 90 min. C_2 concentration profiles inside and outside the shell of (c) Au@Cu_2O-0.5, (d) Au@Cu_2O-1, and (e) Au@Cu_2O-2.Concentrations are shown by color bar in mol m^{-3}. DFT-calculated Gibbs free energy profiles of (f) CO generation pathway on Au (111) and Cu (111) at 0 V and −1.06 V (vs RHE), (g) C-C coupling pathway on Au (111) and Cu (111) at 0 V (vs RHE), (h) formation energetics of key intermediates *CHO, *CHOCO on the Cu (111) surface with a *CO coverage of 0 ML, 1/4, 1/2, 3/4 ML.

confinement of CO generated on Au within the shell, resulting in a higher CO concentration. To rigorously substantiate this hypothesis and further elucidate the reaction mechanism, attenuated total reflection surface-enhanced infrared absorption spectroscopy (ATR-SEIRAS) was employed to monitor the system under various applied potentials, including the optimal operational potential of −1.06 V (vs. RHE) with a duration of 120 min (Fig. 5a and b) of Au@Cu_2O-1 nanoreactors. As the applied potentials shifted negatively, the peaks at 2115 cm^{-1} (linear CO_L) and 1972 cm^{-1} (bridging CO_B) grew more prominent, highlighting the adsorption of CO intermediates, which directly confirmed the abundance of CO intermediates consistent with the observations from Raman spectroscopy [57–59]. Between the two types of *CO, *CO_B was much easier to participate in the hydrogenation reaction due to its weak C=O bond, in contrast to the strong C≡O bond in *CO_L. [60–62] Additionally, a band at 1748 cm^{-1} was attributed to surface-bound *CHO species, a critical intermediate proposed for C-C coupling [63]. The *CHOCO appearance of the bands at 1589 cm^{-1} pointed out the initiation of C-C coupling reactions during the CO_2RR progress [59,64]. The asymmetric *CO-*CHO coupling involving *CHO was a favorable downhill reaction, which was beneficial for C_{2+} products [65]. The intensities of bands assigned to *CHO and *CHOCO intermediates increased from −0.46 V to −1.06 V (vs. RHE). This indicated that *CHOCO was generated from *CHO in the C-C coupling reaction pathway, providing a basis for the subsequent DFT calculations. Moreover, in a 90-min experiment (Fig. 5b), the peak intensities of intermediates remained stable, suggesting the robustness of both the catalytic surface and the reaction process.

3.3.2. Simulation of diffusion and concentration distribution using COMSOL

While in situ spectroscopy effectively tracked intermediate adsorption, it was difficult to fully capture the cascading reactions occurring in Au@Cu_2O nanoreactors or reveal how the relative thicknesses of the Cu_2O shell and hollow layer influenced the diffusion CO and CO_2 as well as C-C coupling progress on the Cu_2O shell. To address these limitations, finite element method (FEM) simulations were conducted to analyze the spatial confinement effects of the Cu_2O shell on *CO intermediates and how the shell-hollow size ratios affected C_{2+} product generation [27,66,67]. Based on the SEM characterization and XPS tests (Fig. 2) after the catalytic reaction, it was observed that Cu_2O remained largely stable during the electrochemical reduction process, thus it was used as the shell material in the model construction. Three Au@Cu_2O models with varying shell-hollow size ratios consistent with the TEM observation (Fig. 1d-f) were constructed to simulate the mass transport of C species under steady-state external CO_2 concentrations. CO_2 molecules diffused through the porous Cu_2O shell to the Au nanoparticles, where they were adsorbed and reduced to *CO. The *CO intermediate either desorbed into the bulk phase as a C_1 intermediate or diffused to the shell surface for C-C coupling to form C_2 products. The density distributions of CO_2, CO, and C_2 were analyzed for the three Au@Cu_2O nanoreactors (Fig. 5c-e and Fig. S14).

Au@Cu_2O-0.5, characterized by the highest shell-hollow size ratio of 2.90, exhibited restricted CO_2 diffusion into the hollow region, resulting in insufficient CO_2 on the Au surface (Fig. 5c). There was not enough CO_2 to generate CO on Au. Consequently, the low CO concentration led to a reduced *CO coverage on Cu_2O, hindering the efficient progression of the C-C coupling process. The significant confinement effect of the relatively large shell thickness in Au@Cu_2O-0.5 extended the diffusion path and residence time of CO within the shell, thereby slightly enhancing C-C coupling. However, the negative impact of CO_2 diffusion hindrance, which reduced CO formation on the Au surface, outweighed the positive impact of CO diffusion limitation in promoting CC coupling. Accordingly, the overall synergistic effect of shell-hollow catalysis resulted in lower CO and C_2 concentrations within the shell compared to Au@Cu_2O-1.

Different from the other two nanoreactors, Au@Cu_2O-1, possessing a tailored optimal shell-hollow size ratio of 1.84, achieved a balance between CO_2 and CO diffusion (Fig. 5d). Concurrently, its relatively optimal hollow size ensured a higher *CO coverage on Cu, accelerating the C-C coupling process. This design achieved the highest local concentrations of CO and C_2 within the nanoreactor, showcasing its superior catalytic performance. Au@Cu_2O-2, with the smallest shell-hollow size ratio of 1.42, demonstrated shorter diffusion paths, facilitating CO_2 diffusion into the shell at the same time CO desorption into the bulk (Fig. 5e). Because of its relatively large hollow size compared to the shell thickness, CO concentration within the hollow decreased sharply when the same amount of CO was generated on the Au surface. This reduction in CO concentration resulted in lower *CO coverage on Cu_2O, which impeded the C-C coupling process. Consequently, the synergistic effects resulted in Au@Cu_2O-2 exhibiting the lowest concentrations of CO and C_2 within the shell.

To further verify the synergistic effects, the C_2/CO concentration ratios in three different Au@Cu_2O nanoreactors were calculated (Fig. S15). The results showed that Au@Cu_2O-1 had the highest C_2/CO ratio, indicating that a larger proportion of CO generated on Au was converted into C_2. This further demonstrated the advantages of the optimized shell-hollow ratio. Moreover, this trend aligned with the experimental results, which reinforced the credibility of the computational results. The calculations also supplemented the experimentally challenging measurement of CO_2 and CO concentration variations within the shell for the three structures. In conclusion, the simulation findings substantiated that the nanoreactor with an optimized shell-hollow ratio harmonized the mass transport of CO_2 and CO within the shell, meanwhile controlling the relative hollow size to maintain optimal *CO coverage on Cu_2O, thereby facilitating the C-C coupling process. This culminated in the maximization of synergistic effects, thereby yielding the most superior electrocatalytic performance.

3.3.3. Comparison of reaction pathways and energy barriers under different CO coverages using DFT calculations

The mass transport of CO_2 and CO within Au@Cu_2O nanoreactors coupled with CO generation on the Au nanoparticles, as well as the hollow size, critically affected the CO concentration in the hollow region. However, probing the influence of CO concentration on the C-C coupling mechanism on Cu_2O through in situ spectroscopy and FEM simulations presented certain challenges. Consequently, we employed DFT calculations to validate these findings rigorously and investigated the effect of *CO surface coverage on the reaction energy barriers at the Cu (111) interface. Based on HRTEM and XRD images, surface models of Au (111) and Cu (111) were constructed to evaluate the adsorption configurations of intermediates. Energy barrier analysis revealed that at −1.06 V (vs. RHE, corresponding to 500 mA cm^{-2}), the formation energy of *COOH (the rate-determining step) on Au (111) (0.33 eV) was lower than the desorption energy of *CO (the rate-determining step) on Cu (111) (0.42 eV), highlighting the superior CO production capability of Au under negative potentials (Fig. 5f). This implied that CO formation predominantly occurred on Au. The energy analysis in this section also supported the previous COMSOL assumption that CO_2 conversion to CO occurred only on Au. Additionally, Au (111) exhibited a lower *CO binding energy and higher *CHO formation and C-C coupling energy barriers than Cu (111) (Fig. 5g). This suggested that in Au@Cu_2O nanoreactors, CO tended to spill over from the Au into the hollow region rather than forming C_2 products on the Au.

From the COMSOL results, it was evident that different shell-hollow ratios led to varying CO concentrations in the hollow region, which affected the CO coverage on Cu_2O and consequently altered the C_2 concentration inside the shell. However, the COMSOL process was unable to capture the reaction pathway of CO forming C_2 from an energy perspective, nor could it reflect the differences in reaction pathway energy barriers under different CO coverage conditions.

To further investigate the effect of *CO coverage on the Cu (111) surface reaction mechanism, four systems with coverages of 0 ML, 1/4

ML, 1/2 ML, and 3/4 ML were analyzed. Meanwhile, based on the *CO, *CHO, and *CHOCO intermediates obtained from ATR-SEIRAS, we established the C-C coupling reaction pathway in which CO(g) in the hollow region combined with *CHO to form *CHOCO (*CHO + CO (aq) → *CHOCO + OH^-(aq)). As depicted in Fig. S16, in the absence of *CO coverage on the Cu (111) surface, *CO was readily desorbed to form CO products. However, with increasing CO coverage, *CO became progressively more hindered in desorption, thereby promoting its subsequent coupling to yield C_{2+} products. For the Cu(111)-1/2 ML system, the energy of the rate-determining step for *CHOCO formation (0.049 eV) was lower than that for the energy of the rate-determining step of 0 ML system (0.172 eV), 1/4 ML system (0.108 eV), and 3/4 ML system (0.083 eV) (Fig. 5h) [68]. These results indicated that moderate *CO coverage facilitates the C-C coupling process, thereby enhancing the C_{2+} product selectivity in the Au@Cu_2O-1 nanoreactor with 1/2 ML coverage. This agreed with previous observations, which indicated that a moderate increase in external CO concentration promotes *CO adsorption and facilitates *CHO–CO coupling within the outer Helmholtz layer [69].

4. Conclusion

Au@Cu_2O nanoreactors with tunable shell-hollow size ratios are synthesized by employing seed growth and Ostwald ripening techniques. Among the three Au@Cu_2O nanoreactors, Au@Cu_2O-1 displays the highest faradaic efficiency for C_{2+} products, demonstrating the synergistic effects of shell-hollow confinement catalysis influenced on CO_2RR to C_{2+}. Notably, Au@Cu_2O-1 achieves a high C_{2+} selectivity with an FE_{C2+} of 76.08% under 500 mA cm^{-2}. ATR-SEIRAS experiments confirm the formation of key intermediates (*CHO and *CHOCO), and finite element method (FEM) simulations reveal the relationship between confined catalysis and structural optimization. The optimized structure of Au@Cu_2O-1 governs the relative diffusion dynamics of CO_2 and CO, CO coverage, as well as the kinetics of the C-C coupling reaction on the shell surface, ensuring superior C_{2+} selectivity. Furthermore, density functional theory (DFT) calculations provide deeper insights into how increased Cu (111) surface *CO coverage lowers the formation energies of *CHO and *CHOCO. This study underscores the pivotal role of shell-hollow confinement in CO_2RR and offers valuable guidance for designing and understanding confined catalysis in cascade nanoreactors.

CRediT authorship contribution statement

Wenqing Chu: Writing – review & editing, Writing – original draft, Visualization, Validation, Methodology, Investigation, Formal analysis, Data curation, Conceptualization. **Guangxin Sun:** Writing – review & editing, Methodology, Conceptualization. **Zheng Chen:** Writing – review & editing. **Xiongwei Tian:** Writing – review & editing. **Shun Wang:** Writing – review & editing. **Mengyin Xie:** Writing – review & editing. **Ruoyu Wu:** Writing – review & editing. **Haijiao Xie:** Software. **Yuqun Zhuo:** Writing – review & editing, Visualization, Validation, Supervision, Resources, Methodology, Funding acquisition.

Declaration of competing interest

The authors declare that they have no known competing financial interests or personal relationships that could have appeared to influence the work reported in this paper.

Appendix A. Supplementary data

Supplementary data to this article can be found online at https://doi.org/10.1016/j.cej.2025.165084.

Data availability

Data will be made available on request.

References

[1] K.B. Karnauskas, S.L. Miller, A.C. Schapiro, Fossil fuel combustion is driving indoor CO2 toward levels harmful to human cognition, GeoHealth 4 (5) (2020) e2019GH000237.

[2] S. Chu, Y. Cui, N. Liu, The path towards sustainable energy, Nat. Mater. 16 (1) (2017) 16–22.

[3] J.H. Montoya, L.C. Seitz, P. Chakthranont, A. Vojvodic, T.F. Jaramillo, J. K. Nørskov, Materials for solar fuels and chemicals, Nat. Mater. 16 (1) (2017) 70–81.

[4] H. Shin, K.U. Hansen, F. Jiao, Techno-economic assessment of low-temperature carbon dioxide electrolysis, Nature Sustainability 4 (10) (2021) 911–919.

[5] B. Yang, K. Liu, H. Li, C. Liu, J. Fu, H. Li, J.E. Huang, P. Ou, T. Alkayyali, C. Cai, Y. Duan, H. Liu, P. An, N. Zhang, W. Li, X. Qiu, C. Jia, J. Hu, L. Chai, Z. Lin, Y. Gao, M. Miyauchi, E. Cortés, S.A. Maier, M. Liu, Accelerating CO2 electroreduction to multicarbon products via synergistic electric–thermal field on copper nanoneedles, J. Am. Chem. Soc. 144 (7) (2022) 3039–3049.

[6] Y. Zhou, Y. Liang, J. Fu, K. Liu, Q. Chen, X. Wang, H. Li, L. Zhu, J. Hu, H. Pan, M. Miyauchi, L. Jiang, E. Cortés, M. Liu, Vertical cu Nanoneedle arrays enhance the local electric field promoting C2 hydrocarbons in the CO2 Electroreduction, Nano Lett. 22 (5) (2022) 1963–1970.

[7] A. Rendón-Calle, S. Builes, F. Calle-Vallejo, A brief review of the computational modeling of CO2 electroreduction on Cu electrodes, Curr. Opin. Electrochem. 9 (2018) 158–165.

[8] P.B. O'Mara, P. Wilde, T.M. Benedetti, C. Andronescu, S. Cheong, J.J. Gooding, R. D. Tilley, W. Schuhmann, Cascade reactions in nanozymes: spatially separated active sites inside Ag-core–porous-Cu-shell nanoparticles for multistep carbon dioxide reduction to higher organic molecules, J. Am. Chem. Soc. 141 (36) (2019) 14093–14097.

[9] T. Yan, X. Chen, L. Kumari, J. Lin, M. Li, Q. Fan, H. Chi, T.J. Meyer, S. Zhang, X. Ma, Multiscale CO2 Electrocatalysis to C2+ products: reaction mechanisms, catalyst design, and device fabrication, Chem. Rev. 123 (17) (2023) 10530–10583.

[10] T.K. Todorova, M.W. Schreiber, M.J.A.C. Fontecave, Mechanistic understanding of CO2 reduction reaction (CO2RR) toward multicarbon products by heterogeneous copper-based catalysts 10 (3) (2019) 1754–1768.

[11] S. Jiang, K. Klingan, C. Pasquini, H. Dau, New aspects of operando Raman spectroscopy applied to electrochemical CO2 reduction on Cu foams 150 (4) (2019).

[12] Y. Katayama, F. Nattino, L. Giordano, J. Hwang, R.R. Rao, O. Andreussi, N. Marzari, Y. Shao-Horn, An in situ surface-enhanced infrared absorption spectroscopy study of electrochemical CO2 reduction: selectivity dependence on surface C-bound and O-bound reaction intermediates 123 (10) (2018) 5951–5963.

[13] K.J.P. Schouten, Y. Kwon, C.J.M. van der Ham, Z. Qin, M.T.M. Koper, A new mechanism for the selectivity to C1 and C2 species in the electrochemical reduction of carbon dioxide on copper electrodes, Chem. Sci. 2 (10) (2011).

[14] C. Zhan, F. Dattila, C. Rettenmaier, A. Bergmann, S. Kühl, R. García-Muelas, N. López, B.R. Cuenya, Revealing the CO coverage-driven C–C coupling mechanism for electrochemical CO2 reduction on Cu2O nanocubes via operando raman spectroscopy, ACS Catalysis 11 (13) (2021) 7694–7701.

[15] T. Zhang, J.C. Bui, Z. Li, A.T. Bell, A.Z. Weber, J. Wu, Highly selective and productive reduction of carbon dioxide to multicarbon products via in situ CO management using segmented tandem electrodes, Nature Catalysis 5 (3) (2022) 202–211.

[16] M. Schreier, Y. Yoon, M.N. Jackson, Y.J.A.C. Surendranath, Competition between H and CO for active sites governs copper-mediated electrosynthesis of hydrocarbon fuels 130 (32) (2018) 10378–10382.

[17] Y. Cai, R. Yang, J. Fu, Z. Li, L. Xie, K. Li, Y.-C. Chang, S. Ding, Z. Lyu, J.-R. Zhang, J.-J. Zhu, Y. Lin, W. Zhu, Self-pressurizing nanoscale capsule catalysts for CO2 electroreduction to acetate or propanol, Nature Synthesis 3 (7) (2024) 891–902.

[18] C. Chen, Y. Li, S. Yu, S. Louisia, J. Jin, M. Li, M.B. Ross, P. Yang, Cu-ag tandem catalysts for high-rate CO₂ electrolysis toward multicarbons, Joule 4 (8) (2020) 1688–1699.

[19] P. Iyengar, M.J. Kolb, J.R. Pankhurst, F. Calle-Vallejo, R. Buonsanti, Elucidating the facet-dependent selectivity for CO2 Electroreduction to ethanol of cu–ag tandem catalysts, ACS Catalysis 11 (8) (2021) 4456–4463.

[20] P. Shao, H.X. Zhang, Q.L. Hong, L. Yi, Q.H. Li, J. Zhang, Enhancing CO_2 electroreduction to ethylene via copper−silver tandem catalyst in boron-imidazolate framework nanosheet, Adv. Energy Mater. 13 (19) (2023).

[21] H. Jia, Y. Yang, T.H. Chow, H. Zhang, X. Liu, J. Wang, C.-Y. Zhang, Symmetry-broken Au–Cu heterostructures and their tandem catalysis process in electrochemical CO_2 reduction, Adv. Funct. Mater. 31 (27) (2021), 2101255.

[22] Y. Zheng, J. Zhang, Z. Ma, G. Zhang, H. Zhang, X. Fu, Y. Ma, F. Liu, M. Liu, H. Huang, Seeded growth of gold–copper janus nanostructures as a tandem catalyst for efficient electroreduction of CO2 to C2+ products, Small 18 (19) (2022) 2201695.

[23] H.S. Jeon, J. Timoshenko, F. Scholten, I. Sinev, A. Herzog, F.T. Haase, B. Roldan Cuenya, Operando insight into the correlation between the structure and composition of CuZn nanoparticles and their selectivity for the electrochemical CO2 reduction, J. Am. Chem. Soc. 141 (50) (2019) 19879–19887.

[24] W. Luo, J. Zhang, M. Li, A. Züttel, Boosting CO production in Electrocatalytic CO2 reduction on highly porous Zn catalysts, ACS Catalysis 9 (5) (2019) 3783–3791.

[25] P. Lu, Q. Chen, G. Yang, L. Tan, X. Feng, J. Yao, Y. Yoneyama, N. Tsubaki, Space-confined self-regulation mechanism from a capsule catalyst to realize an ethanol direct synthesis strategy, ACS Catalysis 10 (2) (2020) 1366–1374.

[26] D. Ren, J. Gao, L. Pan, Z. Wang, J. Luo, S.M. Zakeeruddin, A. Hagfeldt, M. Grätzel, Atomic layer deposition of ZnO on CuO enables selective and efficient Electroreduction of carbon dioxide to liquid fuels, Angew. Chem. Int. Ed. 58 (42) (2019) 15036–15040.

[27] P.-P. Yang, X.-L. Zhang, F.-Y. Gao, Y.-R. Zheng, Z.-Z. Niu, X. Yu, R. Liu, Z.-Z. Wu, S. Qin, L.-P. Chi, Y. Duan, T. Ma, X.-S. Zheng, J.-F. Zhu, H.-J. Wang, M.-R. Gao, S.-H. Yu, Protecting copper oxidation state via intermediate confinement for selective CO2 Electroreduction to C2+ fuels, J. Am. Chem. Soc. 142 (13) (2020) 6400–6408.

[28] K.D. Yang, W.R. Ko, J.H. Lee, S.J. Kim, H. Lee, M.H. Lee, K.T. Nam, Morphology-directed selective production of ethylene or ethane from CO(2) on a cu Mesopore electrode, Angew. Chem. Int. Ed. Engl. 56 (3) (2017) 796–800.

[29] H. Jung, S.Y. Lee, C.W. Lee, M.K. Cho, D.H. Won, C. Kim, H.-S. Oh, B.K. Min, Y.J. Hwang, Electrochemical fragmentation of Cu2O nanoparticles enhancing selective C–C coupling from CO2 reduction reaction, J. Am. Chem. Soc. 141 (11) (2019) 4624–4633.

[30] T.-T. Zhuang, Z.-Q. Liang, A. Seifitokaldani, Y. Li, P. De Luna, T. Burdyny, F. Che, F. Meng, Y. Min, R. Quintero-Bermudez, C.T. Dinh, Y. Pang, M. Zhong, B. Zhang, J. Li, P.-N. Chen, X.-L. Zheng, H. Liang, W.-N. Ge, B.-J. Ye, D. Sinton, S.-H. Yu, E.H. Sargent, Steering post-C–C coupling selectivity enables high efficiency electroreduction of carbon dioxide to multi-carbon alcohols, Nature Catalysis 1 (6) (2018) 421–428.

[31] Y. Lu, H. Li, H. Sun, J. Zhao, Y. Zhang, Y. Wang, C. Zhu, D. Gao, Y. Tuo, J. Zeng, D. Chen, Z. Yan, Confinement Catalysis of Reaction Intermediates in Ag@Cu2O Cascade Nanoreactors toward Boosted Electrochemical C–C Coupling, ACS Catalysis 14 (19) (2024) 14744–14753.

[32] P. Wang, H. Yang, Y. Xu, X. Huang, J. Wang, M. Zhong, T. Cheng, Q. Shao, Synergized cu/Pb Core/Shell Electrocatalyst for high-efficiency CO2 reduction to C2+ liquids, ACS Nano 15 (1) (2021) 1039–1047.

[33] S. Zhang, S. Zhao, D. Qu, X. Liu, Y. Wu, Y. Chen, W. Huang, Electrochemical reduction of CO2 toward C2 valuables on Cu@Ag core-shell tandem catalyst with tunable shell thickness, Small 17 (37) (2021), 2102293.

[34] J. Li, K. Xu, F. Liu, Y. Li, Y. Hu, X. Chen, H. Wang, W. Xu, Y. Ni, G. Ding, T. Zhao, M. Yu, W. Xie, F. Cheng, Hollow hierarchical Cu2O-derived electrocatalysts steering CO2 reduction to multi-carbon chemicals at low overpotentials, Adv. Mater. 35 (26) (2023) 2301127.

[35] L. Zhang, D.A. Blom, H. Wang, Au–Cu2O Core–Shell Nanoparticles: A Hybrid Metal-Semiconductor Heteronanostructure with Geometrically Tunable Optical Properties, Chem. Mater. 23 (20) (2011) 4587–4598.

[36] S. Shen, X. Peng, L. Song, Y. Qiu, C. Li, L. Zhuo, J. He, J. Ren, X. Liu, J. Luo, AuCu alloy nanoparticle embedded Cu submicrocone arrays for selective conversion of CO_2 to ethanol, Small 15 (37) (2019) 1902229.

[37] Y. Zang, T. Liu, P. Wei, H. Li, Q. Wang, G. Wang, X. Bao, Selective CO2 Electroreduction to ethanol over a carbon-coated CuO catalyst, Angew. Chem. Int. Ed. 61 (40) (2022) e202209629.

[38] X. Ma, Y. Shen, S. Yao, C. An, W. Zhang, J. Zhu, R. Si, C. Guo, C. An, Core–shell nanoporous AuCu3@au monolithic electrode for efficient electrochemical CO2 reduction, J. Mater. Chem. A 8 (6) (2020) 3344–3350.

[39] Y. Gao, Q. Wu, X. Liang, Z. Wang, Z. Zheng, P. Wang, Y. Liu, Y. Dai, M.-H. Whangbo, B. Huang, Cu2O nanoparticles with both {100} and {111} facets for enhancing the selectivity and activity of CO2 electroreduction to ethylene, Adv. Sci. 7 (6) (2020), 1902820.

[40] J. Li, Y. Chen, B. Yao, W. Yang, X. Cui, H. Liu, S. Dai, S. Xi, Z. Sun, W. Chen, Cascade dual sites modulate local CO coverage and hydrogen-binding strength to boost CO2 electroreduction to ethylene 146 (8) (2024) 5693–5701.

[41] Q. Sun, X. Tan, C. Jia, C. Rong, S. Wang, C. Han, Y. Xiao, H. Qi, S.C. Smith, C.J.A.F. M. Zhao, Molecule doping of atomically dispersed Cu–Au alloy for enhancing electroreduction of CO to C2+ products 34 (48) (2024) 2406281.

[42] Y. Yan, H. Wang, X. Bi, Y. Zhao, W. Wang, M.J.E. Wu, Tandem catalysts CuSe/AuX for increasing local* CO concentration to promote the photocatalytic CO2 reduction to C2H4 1 (1) (2023) e3.

[43] Z. Wei, S. Yue, S. Gao, M. Cao, R. Cao, Synergetic effects of gold-doped copper nanowires with low au content for enhanced electrocatalytic CO2 reduction to multicarbon products, Nano Res. 16 (5) (2023) 7777–7783.

[44] Z. Wei, W. Wang, T. Shao, S. Yang, C. Liu, D. Si, R. Cao, M. Cao, Constructing ag/cu (2)O Interface for efficient neutral CO(2) Electroreduction to C(2)H(4), Angew. Chem. Int. Ed. Engl. 64 (4) (2025) e202417066.

[45] Y. Yan, H. Zhou, T. Li, D. Wang, P. Schaaf, G. Guo, X. Wang, Bimetallic tandem strategy for effective modulation of CO(2) electrocatalytic selectivity on relatively inert Cu interfaces, Small (2025) e2501125.

[46] R. Wang, Y. Liu, Y. Kong, Q. Chen, S. Zhao, Stabilization of Cu2O catalyst via strong electronic interaction for selective electrocatalytic CO2 reduction to ethanol, Chem. Eng. J. 499 (2024).

[47] R. Zhang, J. Zhang, Y. Song, Y. Yang, M. Li, Y. Zhao, Y. Teng, B. Han, Z. Chen, Cu2O Nano-Homojunction for high-efficiency Electrocatalytic CO2-to-ethylene conversion, Angew. Chem. Int. Ed. Engl. (2025) e202501554.

[48] L. Xiong, X. Zhang, L. Chen, Z. Deng, S. Han, Y. Chen, J. Zhong, H. Sun, Y. Lian, B. Yang, X. Yuan, H. Yu, Y. Liu, X. Yang, J. Guo, M.H. Rummeli, Y. Jiao, Y. Peng, Geometric modulation of local CO flux in ag@cu(2) O Nanoreactors for steering the CO(2) RR pathway toward high-efficacy methane production, Adv. Mater. 33 (32) (2021) e2101741.

[49] X. Wu, X. Li, J. Lv, X. Lv, A. Wu, Z. Qi, H.B. Wu, Pulsed electrolysis promotes CO(2) reduction to ethanol on Heterostructured cu(2)O/ag catalysts, Small 20 (12) (2024) e2307637.

[50] R. Du, Q. Wu, S. Zhang, P. Wang, Z. Li, Y. Qiu, K. Yan, G.I.N. Waterhouse, P. Wang, J. Li, Y. Zhao, W.W. Zhao, X. Wang, G. Chen, CuC(O) interfaces deliver remarkable selectivity and stability for CO(2) reduction to C(2+) products at industrial current density of 500 mA cm(−2), Small 19 (28) (2023) e2301289.

[51] Y. Wang, P. Han, X. Lv, L. Zhang, G. Zheng, Defect and Interface engineering for aqueous Electrocatalytic CO2 reduction, Joule 2 (12) (2018) 2551–2582.

[52] Z. Yan, P. Gao, Z. Li, Y. Zhang, C. Hu, D. Cao, D. Cheng, Rational design and validation of Cu(2)O/Cu heterogeneous interface catalyst for CO(2) electroreduction to C(2+) products, Small (2025) e2500950.

[53] Q. Wu, R. Du, P. Wang, G.I.N. Waterhouse, J. Li, Y. Qiu, K. Yan, Y. Zhao, W.W. Zhao, H.J. Tsai, M.C. Chen, S.F. Hung, X. Wang, G. Chen, Nanograin-boundary-abundant cu(2)O-cu Nanocubes with high C(2+) selectivity and good stability during electrochemical CO(2) reduction at a current density of 500 mA/cm(2), ACS Nano 17 (13) (2023) 12884–12894.

[54] C. Kim, K.M. Cho, K. Park, J.Y. Kim, G.T. Yun, F.M. Toma, I. Gereige, H.T. Jung, Cu/Cu2O interconnected porous aerogel catalyst for highly productive Electrosynthesis of ethanol from CO2, Adv. Funct. Mater. 31 (32) (2021).

[55] R. Zhang, F. Chen, H. Jin, Y. Zhang, X. Hao, Y. Liu, T. Feng, X. Zhang, Z. Lu, W. Wang, F. Lu, H. Dong, H. Liu, H. Liu, Y. Cheng, Highly stability cu+ species in hollow Cu2O nanoreactors by modulating cavity size for CO2 electroreduction to C2+ products, Chem. Eng. J. 461 (2023).

[56] H. Shi, L. Luo, C. Li, Y. Li, T. Zhang, Z. Liu, J. Cui, L. Gu, L. Zhang, Y. Hu, H. Li, C. Li, Stabilizing Cu+ species in Cu2O/CuO catalyst via carbon intermediate confinement for selective CO2RR, Adv. Funct. Mater. 34 (11) (2023).

[57] Y. Deng, A.D. Handoko, Y. Du, S. Xi, B.S. Yeo, In situ Raman spectroscopy of copper and copper oxide surfaces during electrochemical oxygen evolution reaction: identification of CuIII oxides as catalytically active species, ACS Catal. 6 (4) (2016) 2473–2481.

[58] O. Krauth, G. Fahsold, N. Magg, A. Pucci, Anomalous infrared transmission of adsorbates on ultrathin metal films: Fano effect near the percolation threshold, J. Chem. Phys. 113 (15) (2000) 6330–6333.

[59] A. Wuttig, C. Liu, Q. Peng, M. Yaguchi, C.H. Hendon, K. Motobayashi, S. Ye, M. Osawa, Y. Surendranath, Tracking a common surface-bound intermediate during CO2-to-fuels catalysis, ACS Cent. Sci. 2 (8) (2016) 522–528.

[60] J. Ding, F. Li, X. Ren, Y. Liu, Y. Li, Z. Shen, T. Wang, W. Wang, Y.-G. Wang, Y.J.N.C. Cui, Molecular tuning boosts asymmetric CC coupling for CO conversion to acetate 15 (1) (2024), 3641.

[61] P. Wang, H. Yang, C. Tang, Y. Wu, Y. Zheng, T. Cheng, K. Davey, X. Huang, S.-Z.J.N.C. Qiao, Boosting electrocatalytic CO2–to–ethanol production via asymmetric C–C coupling 13 (1) (2022) 3754.

[62] X. Wang, Z. Wang, T.-T. Zhuang, C.-T. Dinh, J. Li, D.-H. Nam, F. Li, C.-W. Huang, C.-S. Tan, Z.J.N.C. Chen, Efficient upgrading of CO to C3 fuel using asymmetric CC coupling active sites 10 (1) (2019) 5186.

[63] G.-Q. Lu, S.-G. Sun, L.-R. Cai, S.-P. Chen, Z.-W. Tian, K.-K. Shiu, In situ FTIR spectroscopic studies of adsorption of CO, SCN-, and poly(o-phenylenediamine) on electrodes of nanometer thin films of Pt, Pd, and Rh: abnormal infrared effects (AIREs), Langmuir 16 (2) (2000) 778–786.

[64] Y. Kim, S. Park, S.-J. Shin, W. Choi, B.K. Min, H. Kim, W. Kim, Y.J. Hwang, Time-resolved observation of C–C coupling intermediates on Cu electrodes for selective electrochemical CO2reduction, Energ. Environ. Sci. 13 (11) (2020) 4301–4311.

[65] J. Gao, H. Zhang, X. Guo, J. Luo, S.M. Zakeeruddin, D. Ren, Grätzel S. M.J.J.O.t.A.C., Selective C–C coupling in carbon dioxide electroreduction via efficient spillover of intermediates as supported by operando Raman spectroscopy 141 (47) (2019) 18704–18714.

[66] F. Yu, X. Liu, L. Liao, G. Xia, H. Wang, Multilayer-cavity tandem catalyst for profiling sequentially coupling of intermediate CO in Electrocatalytic reduction reaction of CO(2) to multi-carbon products, Small 19 (38) (2023) e2301558.

[67] T.-T. Zhuang, Y. Pang, Z.-Q. Liang, Z. Wang, Y. Li, C.-S. Tan, J. Li, C.T. Dinh, P. De Luna, P.-L. Hsieh, T. Burdyny, H.-H. Li, M. Liu, Y. Wang, F. Li, A. Proppe, A. Johnston, D.-H. Nam, Z.-Y. Wu, Y.-R. Zheng, A.H. Ip, H. Tan, L.-J. Chen, S.-H. Yu, S.O. Kelley, D. Sinton, E.H. Sargent, Copper nanocavities confine intermediates for efficient electrosynthesis of C3 alcohol fuels from carbon monoxide, Nat. Catal. 1 (12) (2018) 946–951.

[68] X. Wang, Z. Wang, F.P. García de Arquer, C.-T. Dinh, A. Ozden, Y.C. Li, D.-H. Nam, J. Li, Y.-S. Liu, J. Wicks, Z. Chen, M. Chi, B. Chen, Y. Wang, J. Tam, J.Y. Howe, A. Proppe, P. Todorović, F. Li, T.-T. Zhuang, C.M. Gabardo, A.R. Kirmani, C. McCallum, S.-F. Hung, Y. Lum, M. Luo, Y. Min, A. Xu, C.P. O'Brien, B. Stephen, B. Sun, A.H. Ip, L.J. Richter, S.O. Kelley, D. Sinton, E.H. Sargent, Efficient electrically powered CO2-to-ethanol via suppression of deoxygenation, Nature Energy 5 (6) (2020) 478–486.

[69] X. Wang, J.F. de Araújo, W. Ju, A. Bagger, H. Schmies, S. Kühl, J. Rossmeisl, P. Strasser, Mechanistic reaction pathways of enhanced ethylene yields during electroreduction of CO2–CO co-feeds on Cu and Cu-tandem electrocatalysts, Nat. Nanotechnol. 14 (11) (2019) 1063–1070.